agronomy

Article

Heat Transfer Process of the Tea Plant under the Action of Air Disturbance Frost Protection

Taibai Xu [1], Qingmin Pan [2] and Yongzong Lu [2,*]

[1] Shanghai Vocational College of Agriculture and Forestry, Shanghai 201699, China; xutb@shafc.edu.cn
[2] School of Agricultural Engineering, Jiangsu University, Zhenjiang 212013, China; 2112116011@stmail.ujs.edu.cn
* Correspondence: yzlu@ujs.edu.cn

Abstract: Wind machines based on the air disturbance method are progressively employed to mitigate frost damage within the agricultural machinery frost protection. These devices are utilized during radiative frost nights to disrupt near-surface thermal inversion through air mixing. Despite this application, the fundamental mechanisms underlying these mixing processes are not well comprehended. In this research, numerical simulations were conducted using COMSOL Multiphysics software version 6.0 to simulate the flow and heat transfer processes between the thermal airflow and both the tea canopy and stems. The results indicated that due to obstruction from the canopy cross-section, the airflow velocity on the contact surface rapidly increased. As the airflow further progressed, the high-speed region of the airflow gradually approached the canopy surface. Turbulent kinetic energy increased initially on the windward side of the canopy cross-section and near the top interface. On the windward side of the canopy, due to the initial impact of the thermal airflow, rapid heating occurred, resulting in a noticeable temperature difference between the windward and leeward sides within a short period. In the interaction between airflow and stems, with increasing airflow velocity, fluctuations and the shedding of wake occurred on the leeward side of the stems. The maximum sensible heat flux at the windward vertex of the stem increased significantly with airflow velocity. At an airflow velocity of 2.0 m/s, the maximum heat flux value was 2.37 times that of an airflow velocity of 1.0 m/s. This research utilized simulation methods to study the interaction between airflow and tea canopy and stems in frost protection, laying the foundation for further research on the energy distribution in tea ecosystem under the disturbance of airflow for frost protection.

Keywords: COMSOL simulation; frost protection; heat transfer process; air disturbance

check for updates

Citation: Xu, T.; Pan, Q.; Lu, Y. Heat Transfer Process of the Tea Plant under the Action of Air Disturbance Frost Protection. *Agronomy* **2024**, *14*, 959. https://doi.org/10.3390/agronomy14050959

Academic Editor: Se-Woon Hong

Received: 8 April 2024
Revised: 22 April 2024
Accepted: 30 April 2024
Published: 2 May 2024

1. Introduction

Frost, a meteorological hazard in agriculture, is governed by temperature fluctuations, imposing significant constraints on the sustainable development of agriculture in China. Frost occurs when there is a sudden drop in air temperature, causing a rapid decline in surface temperature to below 0 °C [1–3]. This results in frost damage to the stems, buds, and leaves of crops, potentially leading to crop fatality [4,5]. The ongoing global climate warming trend is diminishing the cold resistance of crops, elevating susceptibility to frost damage. Tea (*Camellia sinensis*) is mainly grown in humid and warm hilly areas, with the survival mainly restricted by freezing temperatures in the late spring [6–9]. However, in recent years, tea cultivation has faced recurrent challenges from frost disasters. The middle and lower reaches of the Yangtze River constitute China's principal regions for cultivating renowned high-quality tea. Frost occurrences in this area primarily stem from radiation frost. Between the years of 2008 and 2022, late spring frosts recurred annually in February and March, resulting in approximately 30% of tea fields experiencing varying degrees of frost damage [8,10,11]. Over the past decade, the climate has exhibited notable variability, leading to frequent occurrences of late spring frosts. For an extended period, various methods have been employed to frost protection, with traditional approaches including bagging, straw covering, field irrigation, and smoke fumigation [9,12–16]. While these methods partially mitigate the harm caused by frost to crops, they suffer from drawbacks such as being time-consuming, resource-intensive, and environmentally polluting [1,2,12]. The use of frost protection wind machines has emerged as an effective technique in frost prevention. Its fundamental principle leverages the temperature inversion phenomenon during frosty nights, where temperatures are higher above and lower below. Mechanical equipment disturbs the air, transporting the warmer upper-level air to the crop canopy. This air then mixes with the cooler air at the canopy, while the continuous mechanical action of the frost protection machine promotes airflow disturbance, thereby raising the temperature at the canopy. This method is also known as the temperature inversion stress method [17–21]. The primary advantage of this frost protection method lies in its efficiency and effectiveness, saving time and effort. In the 20th century, countries such as Japan, the United States, Uruguay, and New Zealand successfully implemented this mechanized frost protection method [2,22]. In the recent two decades, mechanized frost protection equipment such as wind machines and sprinklers have been preliminary applied in China for tea field frost protection, leading to subsequent research on this equipment [23–26].

The process of frost mitigation by wind machine frost protection can be divided into two stages. During period one, wind machines drive warmer air from the inversion layer to the canopy of tea trees, mixing it with the colder air at the canopy to elevate the canopy temperature [18,19,22]. During period two, the hotter air from the inversion layer enhances forced convection between the boundary layer and the crop surface, improving the heat exchange between crops and the environment [27–29].

Recent researchers have predominantly focused on stage one [30–33]. Battany et al. compared the frost protection effectiveness of suction–discharge-type frost protection machines with traditional frost protection wind machines in vineyards [17]. The research found that the temperature rise at a height of 1.1 m above the grapevine under the suction–discharge-type machine was minimal, while under similar conditions, the traditional vertical frost protection wind machine achieved a temperature rise of 1.6 °C, indicating inferior frost protection performance for the suction–discharge-type machine. Heusinkveld et al.'s research demonstrated that natural wind speed can result in asymmetry in frost protection zones, with a larger protected area downwind [34]. Numerical simulations and field experiments showed similar results, with the wind machine's influence area increasing as the rotation time (3–6 min) decreases, while the temperature rise remains relatively constant. Recent research of stage two is relatively scarce. The mechanism of plant thermal effects under the influence of the wind machine, combining microclimate and energy exchange, represents a new direction for future studies on frost protection effectiveness. Kimura et al. suggested that the airflow, once initiated by the frost protection wind machine, directly affects the boundary layer conductivity of the blades [35]. While the airflow from the machine and the surface airflow of the blades exhibit some synchronicity, the temperature difference between the air and the blades is complex, and there is a delayed dynamic thermal response between the blades and the environment. Dai et al. conducted a quantitative 3D investigation of air disturbance frost protection to quantify the magnitude and area of warming by air mixing and identify the characteristic mixing processes downwind and upwind [36]. However, previous studies were concentrated on big-scale analysis and there is no micro-scale study of the transport process and interaction mechanism between cold tea tree and hot air under the action of air disturbance for frost protection.

COMSOL Multiphysics is grounded in the finite element method, utilizing the solution of partial differential equations (single field) or sets of partial differential equations (multi-field) to simulate real-world physical phenomena. Employing mathematical methods, it addresses the simulation of diverse physical processes in scientific research and engineering computations [37–40]. The most commonly used turbulence models are the

Spalart–Allmaras model and k-ε model. However, due to the Spalart–Allmaras model lacking consideration of length-scale variations of tea fields, it may not be suitable for flows with significant changes in flow scale [41]. The *k-ε* model predicted the rate of free shear flow propagation, as observed in wake flows, mixed flows, flow around flat plates, flow around cylinders, and radial jet flows [42]. Consequently, it can be applied to the interaction and energy transfer process between the airflow from the wind machine and the tea canopy, as well as the stem.

Thus, in order to analyze the energy transfer process and the relationship between the air–tea tree–soil system in the air disturbance at frost night, we used the k-ε model coupled with the "non-isothermal flow" multi-physical field interface to simulate the temperature field and flow field distribution around the frost night cold tea canopy under the action of air disturbance under different wind speed conditions. The heat transfer process of airflow around an individual canopy and stalk was calculated and analyzed. It will lay the foundation for further research on the energy distribution in tea ecosystem under the disturbance of airflow for frost protection.

2. Materials and Methods

2.1. Governing Equation Construction

The transport equation for turbulent kinetic energy k in the standard k-ε model is derived through mathematical analysis, while the transport equation for the dissipation rate ε is obtained through physical analysis. The transport equations for k and ε are as follows:

$$\rho\frac{Dk}{Dt} = \frac{\partial}{\partial x_i}\left[\left(\mu + \frac{\mu_t}{\sigma_k}\right)\frac{\partial k}{\partial x_i}\right] + G_k + G_b - \rho\varepsilon - Y_M \tag{1}$$

$$\rho\frac{D\varepsilon}{Dt} = \frac{\partial}{\partial x_i}\left[\left(\mu + \frac{\mu_t}{\sigma_\varepsilon}\right)\frac{\partial \varepsilon}{\partial x_i}\right] + G_{1\varepsilon}\frac{\varepsilon}{k}(G_k + C_{3\varepsilon}G_b) - C_{2\varepsilon}\rho\left(\varepsilon^2/k\right) \tag{2}$$

where G_k is the term for turbulent kinetic energy generation due to velocity gradient; G_b is the term for turbulent kinetic energy generation caused by buoyancy; and Y_M is the expansion term in compressible turbulence. $C_{1\varepsilon}$, $C_{2\varepsilon}$, and $C_{3\varepsilon}$ are the constants. σ_k and σ_ε represent the turbulent Prandtl numbers for k and ε, respectively. The transport equation for the *RNG* k-ε model is similar to that of the standard k-ε model [41], given by

$$\rho\frac{Dk}{Dt} = \frac{\partial}{\partial x_j}\left[\left(\alpha_k\mu_{eff}\frac{\partial k}{\partial x_j}\right)\right] + Gk + Gb - \rho\varepsilon - Y_M \tag{3}$$

$$\rho\frac{D\varepsilon}{Dt} = \frac{\partial}{\partial x_i}\left[\left(\alpha_\varepsilon\mu_{eff}\frac{\partial \varepsilon}{\partial x_i}\right)\right] + C_{1\varepsilon}\frac{\varepsilon}{k}(Gk + C_{3\varepsilon}G_b) - C_{2\varepsilon}\rho\left(\varepsilon^2/k\right) - R \tag{4}$$

where α_k and α_ε are the reverse effective Prandtl numbers for k and ε respectively, and R represents an additional term. The SST k-ω model uses turbulent kinetic energy k and its specific dissipation rate ω as the solving variables [43]. The latter is defined as

$$\omega = \frac{\varepsilon}{\beta^* k} \tag{5}$$

$$\frac{\partial \rho k}{\partial t} + \frac{\partial \rho u_j k}{\partial x_j} = P - \beta^*\rho\omega k + \frac{\partial}{\partial x_j}\left[(\mu + \sigma_k\mu_t)\frac{\partial k}{\partial x_j}\right] \tag{6}$$

$$\frac{\partial \rho\omega}{\partial t} + \frac{\partial \rho u_j}{\partial x_j} = \frac{\gamma}{v_t}P - \beta\rho\omega^2 + \frac{\partial}{\partial x_j}\left[(\mu + \sigma_\omega\mu_t)\frac{\partial \omega}{\partial x_j}\right] + 2(1 - F_1)\frac{\rho\sigma_{\omega^2}}{\omega}\bullet\frac{\partial k}{\partial x_j}\bullet\frac{\partial \omega}{\partial x_j} \tag{7}$$

In the above equation, the first three terms on the right-hand side represent the generation term, dissipation term, and diffusion term, respectively. The fourth term on the right-hand side of the ω equation is the cross-diffusion term. The formula is as follows:

$$P = \tau_{ij}\frac{\partial u_i}{\partial x_i} \tag{8}$$

$$\tau_{ij} = \mu\left(2S_{ij} - \frac{2}{3}\frac{\partial u_k}{\partial x_k}\delta_{ij}\right) - \frac{2}{3}\rho k\delta_{ij} \tag{9}$$

$$S_{ij} = \frac{1}{2}\left(\frac{\partial u_i}{\partial x_j} + \frac{\partial u_j}{\partial x_i}\right) \tag{10}$$

where ε represents the turbulent kinetic energy dissipation rate; ρ is the density; u_j (j = 1, 2, 3) denotes the velocity components; μ is the laminar viscosity, v_t is the turbulent eddy viscosity; v is the molecular viscosity; τ_{ij} represents the viscous shear stress; and $\beta^*, \beta, \gamma, \sigma_k, \sigma_\omega, \sigma_{\omega^2}$ are the closure constants.

When solving for the flow field, the "Solid and Fluid Heat Transfer" module is coupled, and the energy control equation is given by [44]

$$\rho c_p\frac{\partial T}{\partial t} + \rho c_p u \cdot \nabla T + \nabla \cdot q = Q \tag{11}$$

$$q = -k\nabla T \tag{12}$$

where c_p represents the constant pressure specific heat; T is the temperature; Q is the heat; and k is the thermal conductivity.

When solving for the bending process of the stems, the "Solid Mechanics" module is coupled, treating the stems as elastic bodies, and the governing equation is [45]

$$\rho\frac{\partial^2 \chi}{\partial t^2} = \nabla \cdot \sigma + f \tag{13}$$

$$\frac{E}{2(1+v)}\left[\frac{1}{(1-2v)}\nabla(\nabla \cdot \chi) + \nabla^2\chi\right] + f = \rho\frac{\partial^2 \chi}{\partial t^2} \tag{14}$$

where f is the unit volume force; χ represents the solid displacement; E is the elastic modulus; and v is Poisson's ratio.

2.2. Simulation of Fluid–Solid Heat Coupling in the Cross-Section of Tea Plant Rows

2.2.1. Model Configuration and Mesh Independence

During the simulation process, the turbulent *k-w* interface is initially employed to solve the motion and distribution of incompressible fluids. The "Solid and Fluid Heat Transfer" interface is then utilized to address the heat transfer between air and the canopy of tea trees. The coupling between the two interfaces is achieved through the "Non-Isothermal Flow" mechanism, with the mesh being generated using a free triangular grid (as shown in Figure 1). A total of five experimental combinations are set based on the distance from the fan, wind speed, and initial temperature to investigate various scenarios (Table 1).

Table 1. Experimental combination settings with three main factors.

	Distance from the Wind Machine (m)	Velocity (m/s)	Initial Temperature (°C)	Initial Environment Humidity (%)	Initial Wind Speed (m/s)
Case 1	0	0.2	0.2	90.0	0
Case 2	2.7	2.7	0.5	90.0	0
Case 3	3.4	3.4	0.7	90.0	0
Case 4	1.9	1.9	0.5	90.0	0
Case 5	0.6	0.6	1.1	90.0	0

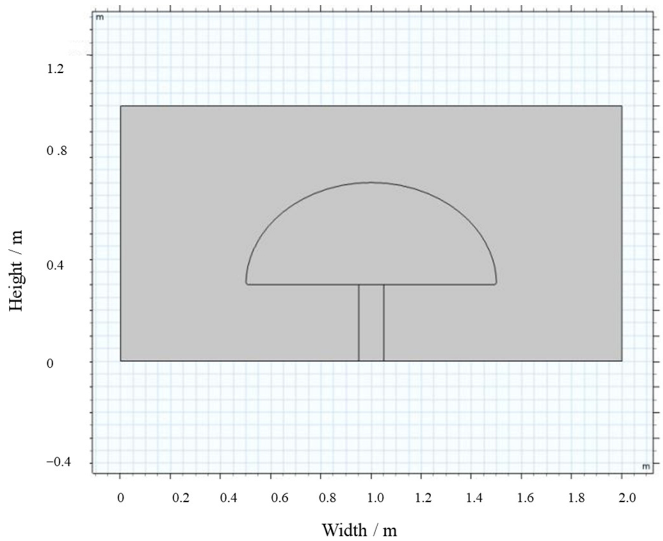

Figure 1. Transient geometric model for calculating the canopy section of tea rows.

2.2.2. Grid Independence Verification

For the steady-state computation of the three-dimensional model, the wind speed was set to 3.0 m/s, the airflow temperature was set to 278.15 K, the environmental temperature was set to 274.15 K, and the initial temperature of the tea tree canopy was set to 270.15 K. The temperature values at the top middle point of the tea rows are shown for five different grid accuracies (Figure 2). With the grid accuracy increased, the temperature gradually raised. Considering computational efficiency, a mesh of 1.998 million elements was chosen for the calculation.

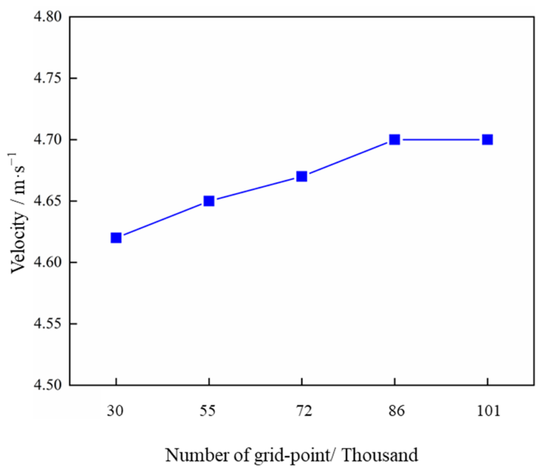

Figure 2. Grid independence verification.

Prior to the transient study, a grid independence check was also conducted. The parameter under consideration is airflow velocity at the canopy vertices. Ultimately, it was determined that 86,000 elements are sufficient for the transient study.

To enhance the convergence of the model, a step function was defined with the impact speed was set as $a \times \text{step1}(t\ [1/\text{s}])$, where a represents the specific velocity magnitude.

2.3. Thermal–Fluid–Structure Coupling Analysis of Stem in Tea Plant Rows

Due to the simulation study and analysis treating the entire canopy of the tea plant rows as a whole in the previous section, the interaction between airflow and tea tree stems could not be fully revealed. Therefore, a two-dimensional model of tea tree stems was established to further analyze the heat exchange phenomena and cylindrical flow between the thermal airflow and the stems.

A two-dimensional cross-section model of the stem was established, starting with a steady-state calculation followed by a transient calculation. In the steady-state calculation, the entire calculation domain size was 1.0×0.4 m, stem diameter was 3.0 cm, a fixed constraint was applied on the leeward side of the stem, and a free condition was applied on the windward side (Figure 3). The inflow velocity perpendicular to the airflow was 1.0 m/s, the initial temperature of the stem was 272.15 K, the initial temperature of the ambient environment around the stem was 273.15 K, and the temperature of the airflow was 278.15 K. The grid uses a free triangular division, and boundary layer thickening was applied around the stem.

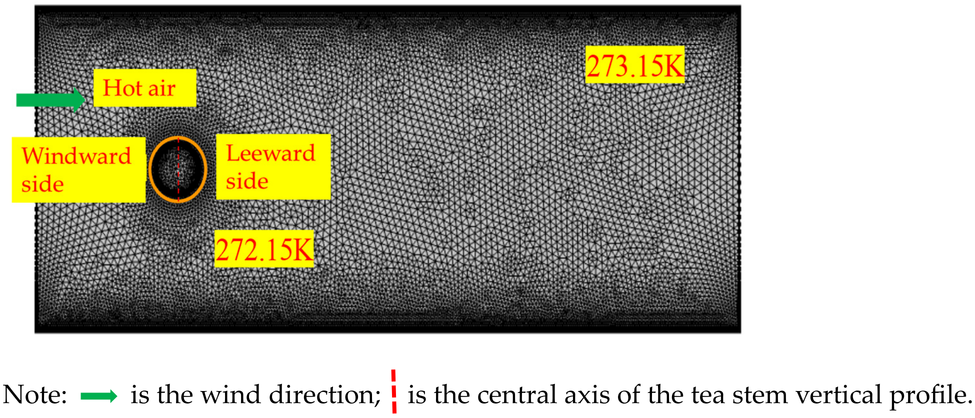

Figure 3. Stem geometry model and initial conditions.

3. Results and Discussion

3.1. The Transient Velocity Distribution of Airflow in the Cross-Section of Tea Rows

The incoming airflow velocity was set to 3.4 m/s. In the initial stage of airflow entry (0.1–0.2 s), the velocity of the airflow contact surface rapidly increased due to obstruction from the canopy cross-section. As the airflow progressed further, the high-speed region of the airflow gradually approached the surface of the canopy (0.3 s). In the subsequent flow, the flow velocity at the top of the canopy gradually stabilized (0.6–2.0 s). At the time of 3.0 s, velocity vortices also appeared in the main stem region below the canopy.

The distribution of turbulent kinetic energy (k) at an incoming airflow velocity of 3.7 m/s is shown in Figure 4. Turbulent kinetic energy represented the rate of change of fluid velocity. It can be observed that under this condition, the turbulent kinetic energy increased first on the windward side of the canopy cross-section and near the top interface of the canopy (0.3 s). As turbulence developed, the value of k at the windward side of the canopy further increased. During the development process from 1.0 s to 5.0 s, the airflow gradually progressed along the surface of the canopy toward the leeward side, and the k value also gradually increased in the leeward region.

Figure 5 presents the variation in the temperature on the top surface of the canopy over time. On the windward side of the canopy, heat exchange occurred first due to the initial impact of the warm airflow, leading to a rapid increase in surface temperature but within a limited range (0.1 s). The temperature on the leeward side remained almost unchanged. As time progressed, the temperature rise value significantly increased, and the range of temperature rise gradually expanded (0.2–0.6 s) (Figure 6). It can also be noted that, within a short period, there was a noticeable temperature difference between the windward and leeward sides of the canopy.

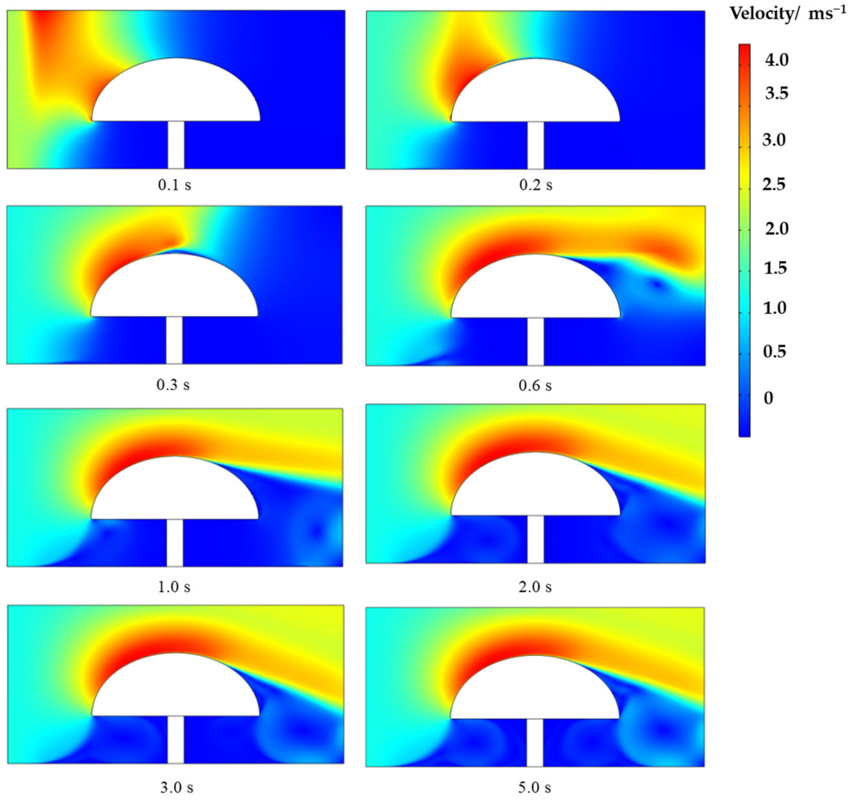

Figure 4. Transient velocity distribution of airflow in the cross-section of tea rows.

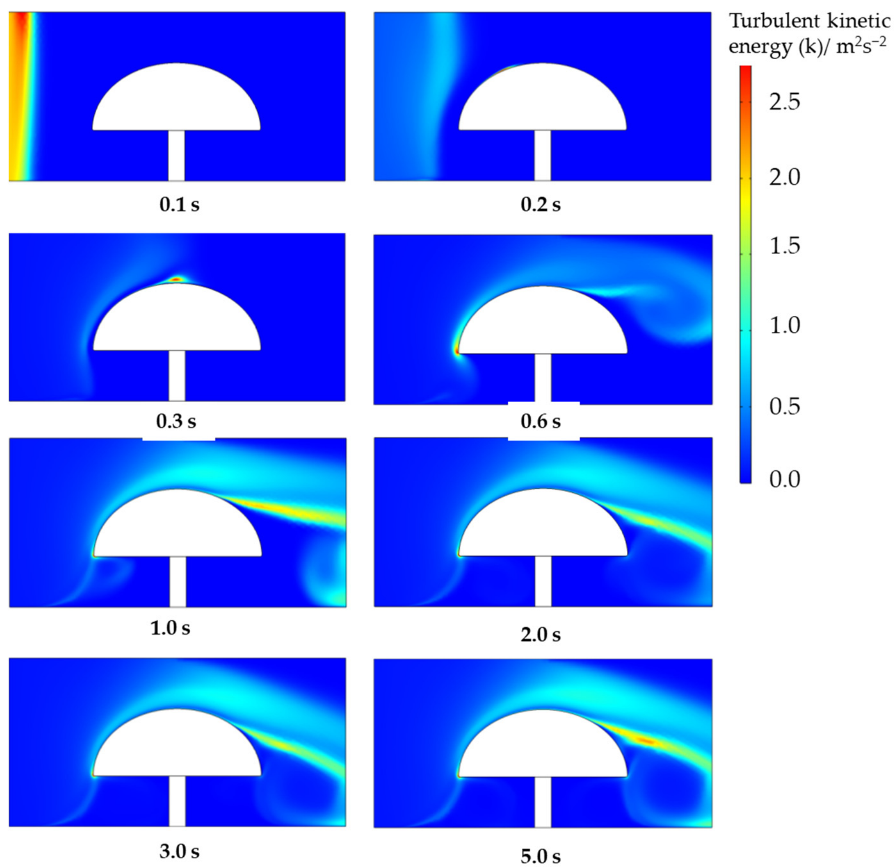

Figure 5. The distribution of turbulent kinetic energy in the cross-section of tea rows.

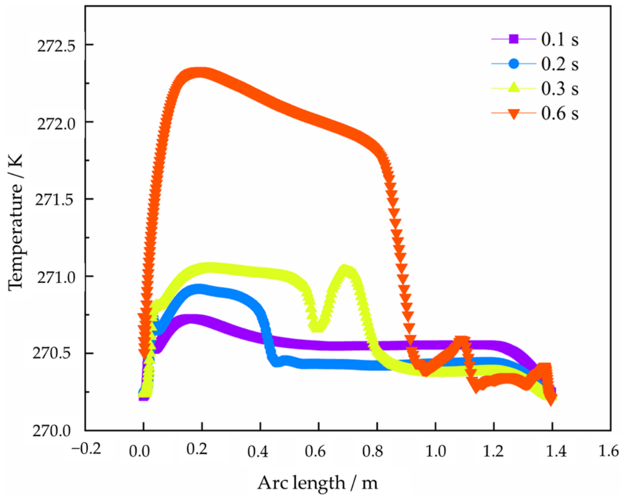

Figure 6. Dynamitic change of the temperature on the top surface of the canopy over the time.

Based on the measured actual airflow velocities at different positions of the fan in the experiment, the influence of airflow velocity on the sensible heat flux on the upper surface of the canopy at the same moment (1.0 s) was calculated and analyzed (Figure 7). It is evident that as the airflow velocity increases, the sensible heat flux on the surface of the canopy gradually increases. Additionally, it can be observed that there is a significant difference in the sensible heat flux on the windward and leeward sides of the canopy at different airflow velocities. This is primarily due to the increase in heat exchange on the windward side with the increase in airflow velocity.

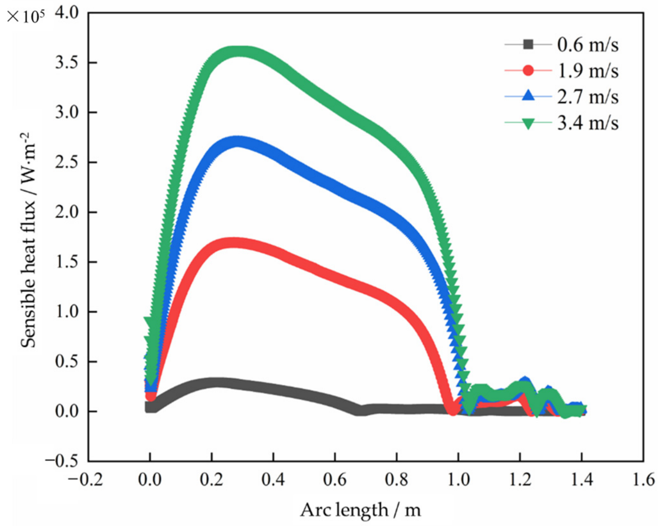

Figure 7. Dynamitic change of sensible heat flux on the top surface of the canopy over the time.

3.2. Simulation Results of the Thermal–Fluid–Structure Coupling of Tea Stems

The steady-state velocity field distribution around the stem is shown in Figure 8. There was a velocity stagnation point on the windward side of the stem, and the velocity magnitude was similar to that on the leeward side, both being relatively small. The airflow velocity reached its maximum on both sides of the stem, with a maximum of 1.4 m/s. The distribution of the steady-state pressure field is shown in Figure 9. Due to the presence of the stem, a high-pressure zone was formed on the windward side of the stem, while a large negative pressure area appeared on the leeward side.

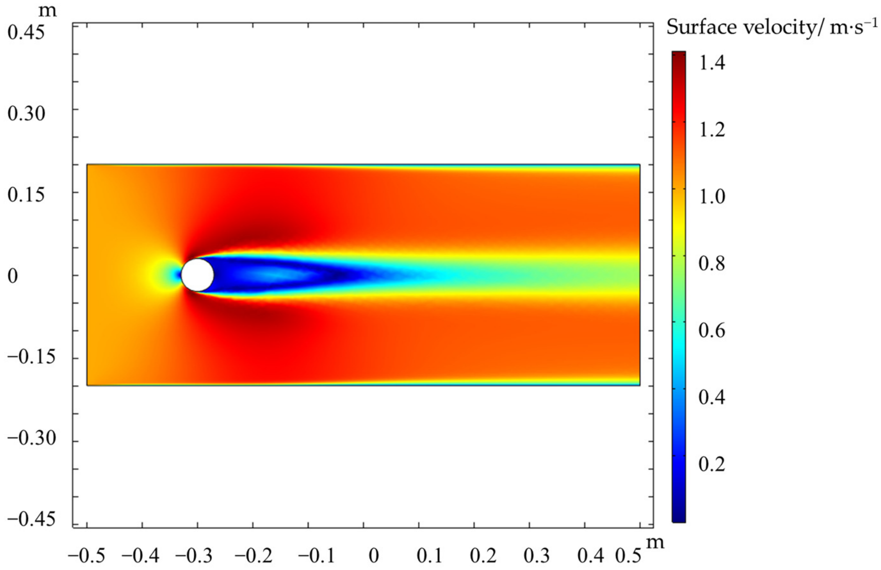

Figure 8. Steady-state velocity distribution.

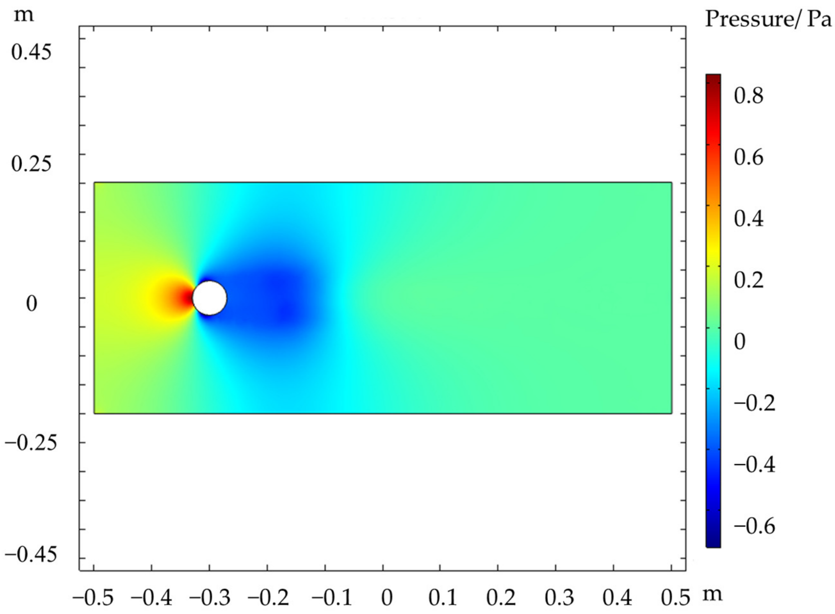

Figure 9. Steady-state pressure distribution.

After reaching a steady state, the temperature field distribution was shown in Figure 10. It can be observed that, under the thermal transmission from the warm airflow, the temperature inside the stem increased with the high-temperature region concentrated on the leeward side of the stem. It clearly indicated that turbulent kinetic energy was concentrated on the leeward side of the stem which formed a vortex-like shape at a certain distance from the stem (Figure 11). In the subsequent transient study, the shedding of Karman vortices occurred in this vicinity.

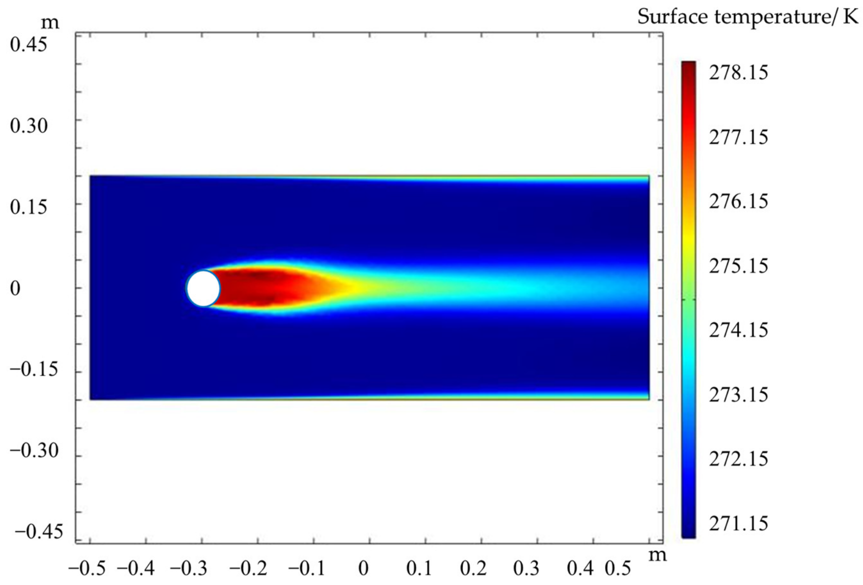

Figure 10. Steady-state temperature distribution.

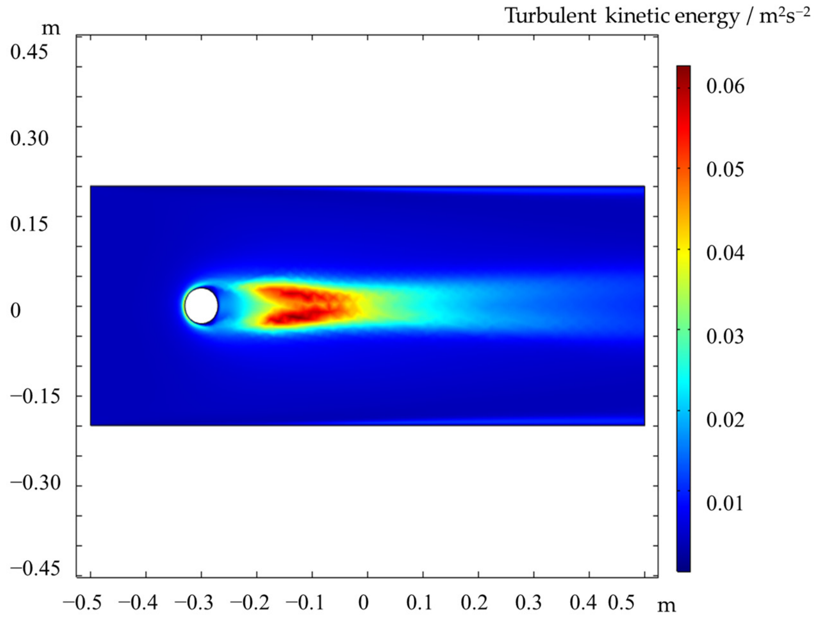

Figure 11. Steady turbulent kinetic energy distribution.

3.3. Transient Analysis of Thermal–Fluid–Structure Coupling with Airflow Disturbance

From the above steady-state results, the influence of the presence of stems on the final flow and temperature distribution in the turbulent field was evident. However, the entire dynamic process cannot be fully revealed. Therefore, transient studies were conducted under the same initial conditions to further analyze the details of the changes in the flow field and temperature field.

During the initial 0.1 s of airflow inflow, the velocity distribution on the windward and leeward sides of the stem were both relatively small, while the airflow velocity near the surfaces on both sides was higher than the initial inflow velocity. At 0.5 s, an asymmetry in the velocity magnitude on the windward and leeward sides became apparent. At 1.5 s, the wake on the leeward side gradually increased. At 2.0 s, the length of the wake further increased but remained stable. At 6.0 s, oscillations appeared at the end of the wake, exhibiting an asymmetrical distribution. With further development, at 10.0 s, a strongly curved flame-like wake can be observed, but there was no occurrence of shedding Karman vortices (Figure 12).

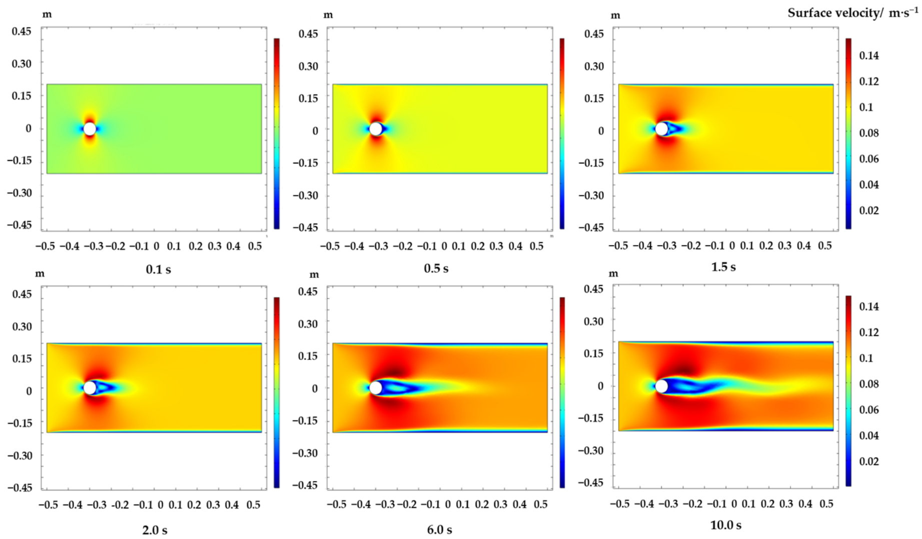

Figure 12. The transient velocity field distribution at an airflow velocity of 0.1 m/s.

The wake in Figure 12 initially exhibited a symmetric pattern and gradually underwent oscillations. The pressure distribution results revealed that when the airflow passes over the surface of the stem (1.0 s), two negative pressure regions appeared on either side at the downstream positions (Figure 13). As the airflow further developed, these two negative pressure regions gradually extended backward. At 4.0 s, these two negative pressure regions became asymmetric, and in the subsequent time period (4.0–6.0 s), the sizes of the two negative pressure regions alternately changed. This alternation led to the oscillation of the wake.

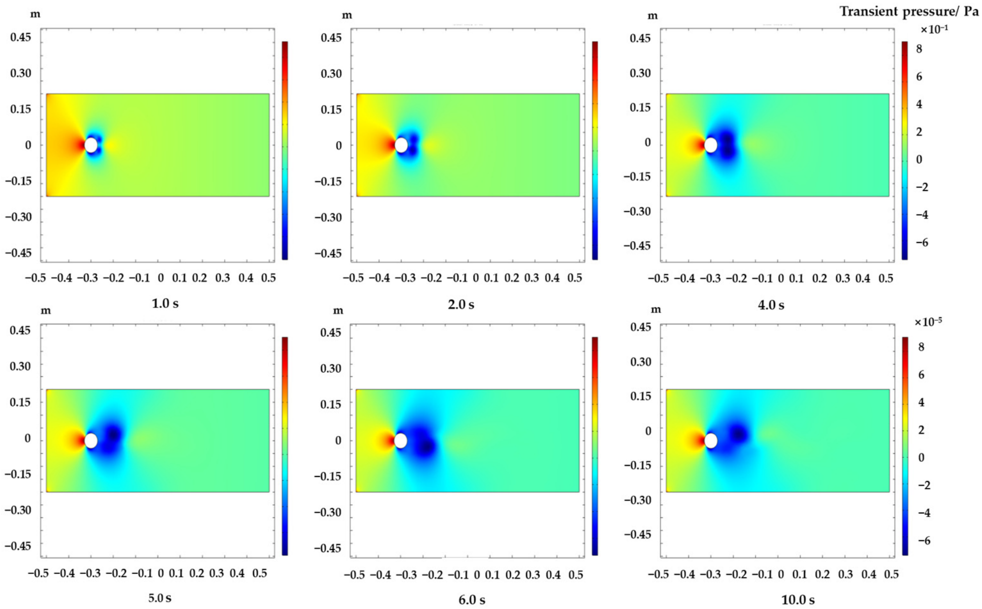

Figure 13. The transient pressure distribution at an airflow velocity of 0.1 m/s.

In Figure 14, the temperature variation around the stem at an airflow velocity of 0.1 m/s is presented. Due to the short duration, the temperature of the stem increased during the transient period but did not reach a stable state. From 1.0 s to 2.0 s, as the warm airflow gradually touched the stem, the temperature distribution significantly increased. At

4.0 s, it can be observed that the high-temperature airflow rapidly extended backward, but a stable and elongated low-temperature region appeared in the middle. In the subsequent time (6.0–10.0 s), instantaneous temperatures gradually exhibited turbulent distribution further away from the stem. The heat flux at the windward side vertex of the stem gradually increased in the early stage (Figure 15). As the airflow further developed, influenced by turbulent flow, the heat flux at this point also underwent significant fluctuations, but the maximum heat flux remained relatively stable.

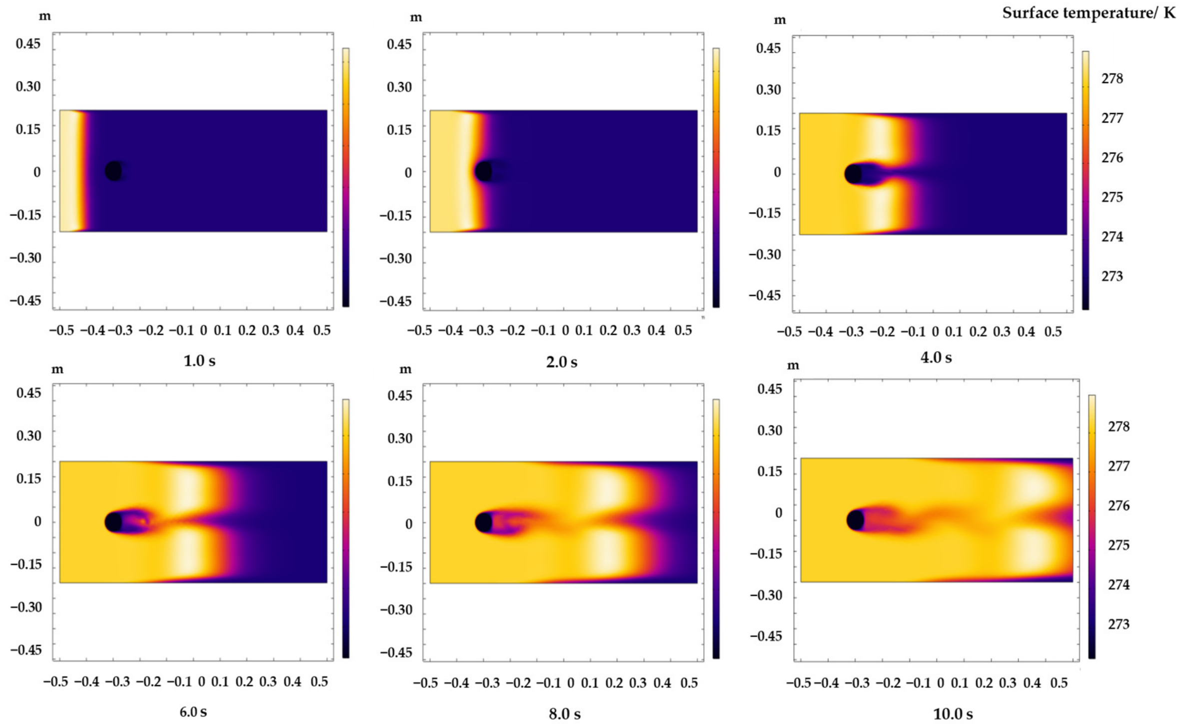

Figure 14. The transient temperature distribution at an airflow velocity of 0.1 m/s.

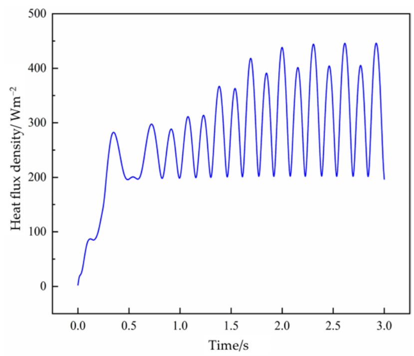

Figure 15. The heat flux at the windward side vertex.

3.4. The Influence of Airflow Velocity

When the airflow velocity increased to 1.0 m/s, the airflow distribution exhibited a faster development of the wake on the leeward side of the stem compared to the airflow velocity of 0.1 m/s. Additionally, at 2.0 s, it can be observed that the wake underwent vigorous oscillations, leading to the occurrence of Karman vortex shedding phenomenon (Figure 16).

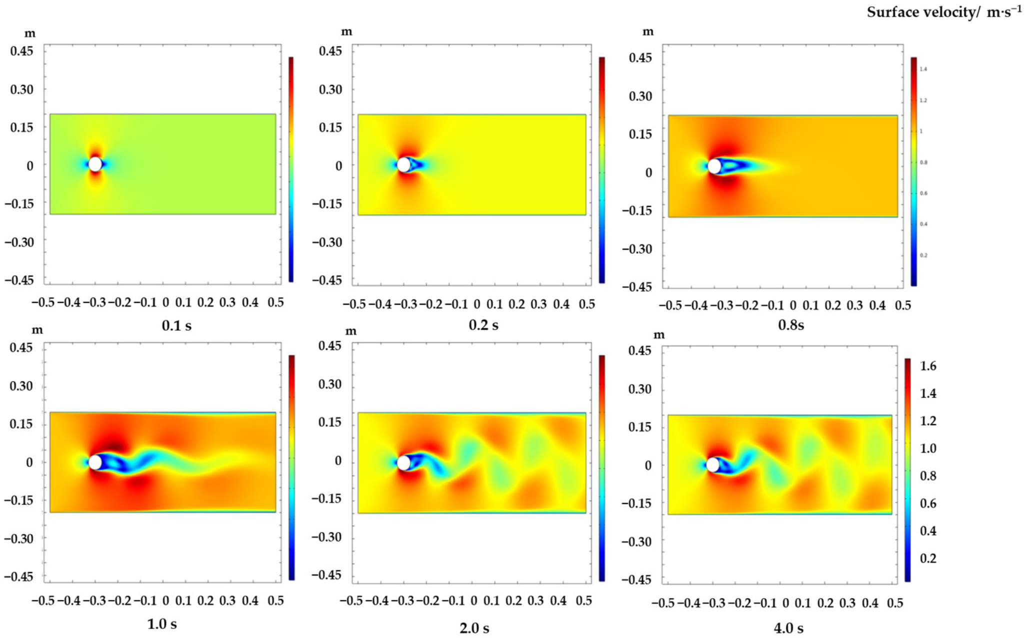

Figure 16. Transient velocity distribution at an airflow velocity of 1.0 m/s.

It can be observed that in the initial stage of airflow entry, the pressure field was symmetric. However, within a very short period (0.8 s), a significantly asymmetric distribution of negative pressure zones appeared, and the difference in size between the two regions was larger than at an airflow velocity of 0.1 m/s. As turbulence further developed, indicating the vigorous oscillation of the wake, the size of the negative pressure zones markedly decreased (Figure 17).

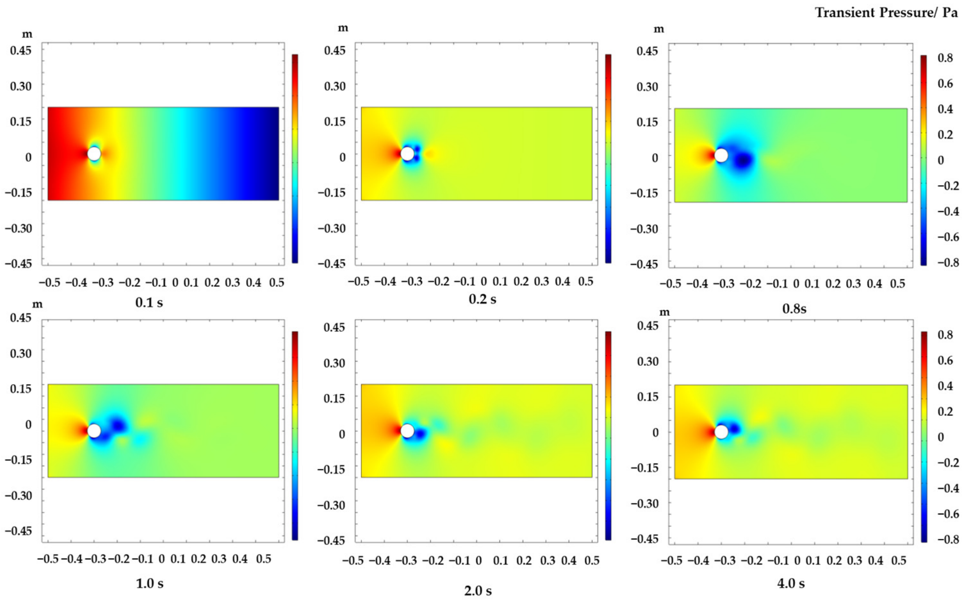

Figure 17. Transient pressure distribution at an airflow velocity of 1.0 m/s.

When the airflow velocity was 1.0 m/s, the temperature distribution characteristics are shown in Figure 18. The mixing on the leeward side of the stem was more intense, and the temperature showed a significant increase. The temperature distribution within the calculation domain was also more uniform compared to when the airflow was 0.1 m/s, and the temperature rise was more pronounced.

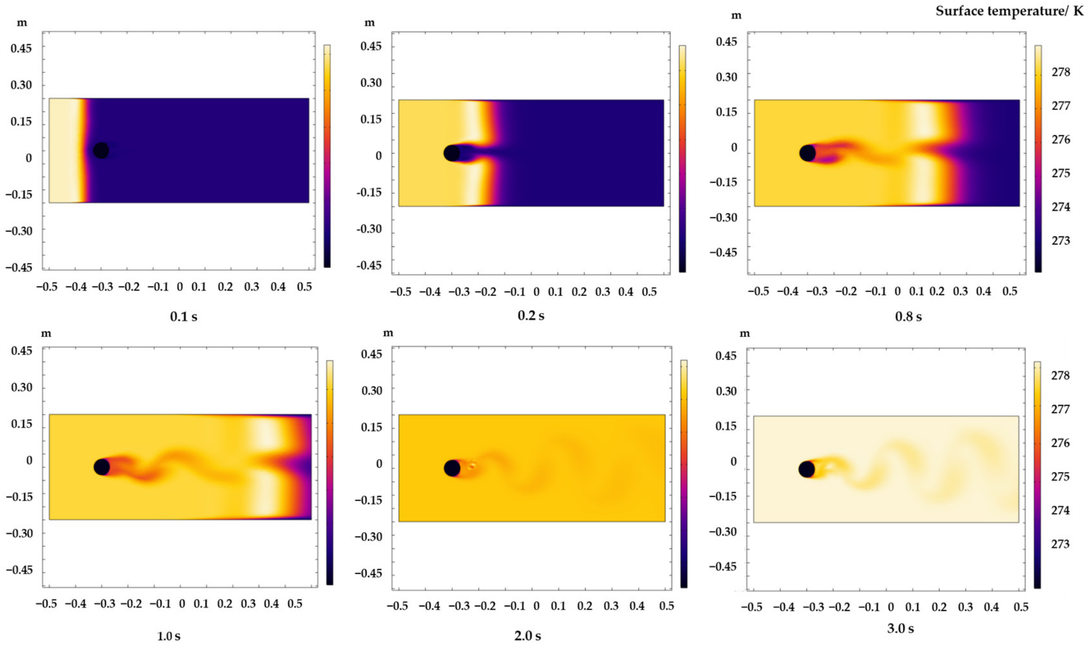

Figure 18. Transient temperature distribution at an airflow velocity of 1.0 m/s.

Figure 19 presented the variation in the maximum heat flux at the leeward side vertex of the stem with airflow velocity. It can be observed that with the increase in airflow velocity, the maximum heat flux at the leeward side vertex of the stem significantly increased. For instance, when the airflow velocity was 2.0 m/s, the maximum heat flux value was 2.37 times that at an airflow velocity of 1.0 m/s.

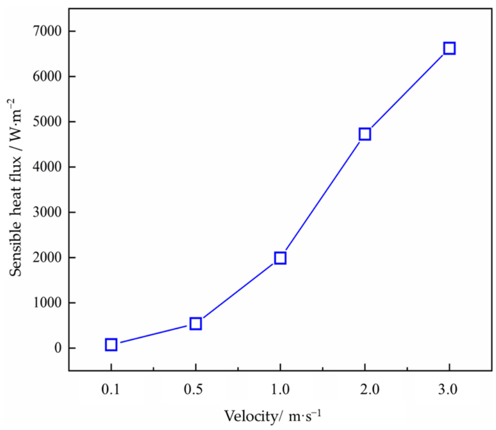

Figure 19. Maximum sensible heat flux at the top of the windward under different airflow velocities.

3.5. The Influence of the Stem Diameter

Figure 20 presents the velocity distribution when the stem diameter is 0.02 m. The formation of the wake and the shedding process of the Karman vortex street were similar to the previous description. However, as the stem diameter changed, the width of the wake also had a noticeable variation. When the stem diameter decreased to 0.02 m, the width of the wake significantly decreased, and its oscillation amplitude also decreased markedly. It illustrated the influence of different stem diameters on turbulent airflow kinetic energy at the same moment (Figure 21). With an increase in stem diameter, the numerical value of turbulent kinetic energy noticeably increased.

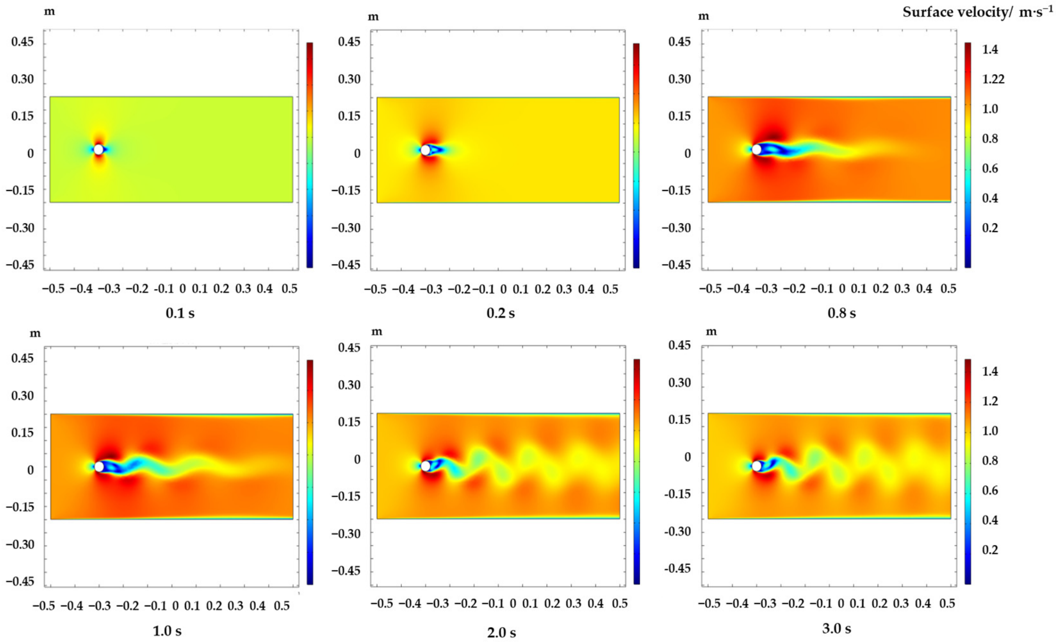

Figure 20. Velocity distribution with the stem diameter of 0.02 m.

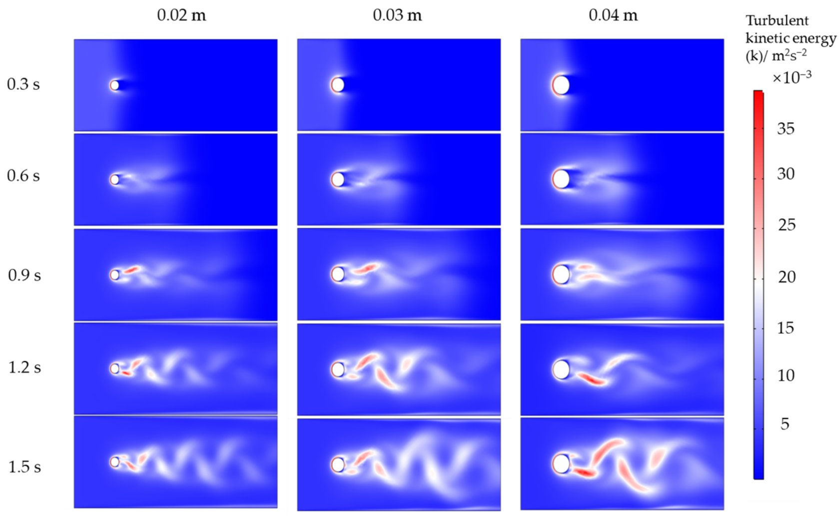

Figure 21. Influence of the stem diameter on turbulent kinetic energy.

4. Conclusions

In this research, numerical simulations were conducted using COMSOL Multiphysics software version 6.0 to simulate the flow and heat transfer processes between the thermal airflow and both the tea canopy and stems. In order to analyze the energy transfer process and the relationship between the air–tea tree–soil system in the air disturbance at frost night, the k-ε model coupled with the "non-isothermal flow" multi-physical field interface was used to simulate the temperature field and flow field distribution around the frost night cold tea canopy under the action of air disturbance under different wind speed conditions. The heat transfer process of airflow around an individual canopy and stalk was calculated and analyzed.

Due to obstruction from the canopy cross-section, the airflow velocity on the contact surface rapidly increased. As the airflow further progressed, the high-speed region of the airflow gradually approached the canopy surface. Turbulent kinetic energy increased initially on the windward side of the canopy cross-section and near the top interface. On the windward side of the canopy, due to the initial impact of the thermal airflow, rapid heating occurred, resulting in a noticeable temperature difference between the windward and leeward sides within a short period.

In the interaction between airflow and stems, with an increasing airflow velocity, fluctuations, and shedding of wake occurred on the leeward side of the stems. The maximum sensible heat flux at the windward vertex of the stem increased significantly with airflow velocity. At an airflow velocity of 2.0 m/s, the maximum heat flux value was 2.37 times than that at an airflow velocity of 1.0 m/s. This research utilized simulation methods to study the interaction between airflow and tea canopy and stems in frost protection, laying the foundation for further research on the energy distribution in tea ecosystem under the disturbance of airflow for frost protection.

In the model establishment, the size of the tea tree model, different wind speed, and initial temperature were obtained from the actual field environment, and the process of frost protection was based on the real frost protection scene. In the future, we will focus on the field research of evaluating the heat transfer process of the tea plant to verify the temperature distribution under air disturbance frost protection. On the other hand, tea plant is a very complex system with different sizes of branches and leaves. In future research, we will focus on the consequence of mutual influence on the formation of airflows and heat exchange with different characteristics of tea.

Author Contributions: T.X. and Y.L. conceived and designed the experiments. T.X., Q.P. and Y.L. performed the experiments and analyzed the data. Y.L. wrote the manuscript. T.X. and Y.L. gave some significant comments to improve the quality and language of the manuscript. All authors have read and agreed to the published version of the manuscript.

Funding: This research was funded by the project of Jiangsu Province and Education Ministry Co-Sponsored Synergistic Innovation Center of Modern Agricultural Equipment (XTCX2013), the Project of Postgraduate Innovation of Jiangsu Province (KYCX22_3683), the Academic Program Development of Jiangsu Higher Education Institutions (PAPD-2023-87), and the Academic Program of Shanghai Vocational College of Agriculture and Forestry (KY6-0000-24-10).

Data Availability Statement: The original contributions presented in the study are included in the article, further inquiries can be directed to the corresponding author.

Acknowledgments: We sincerely appreciate the School of Agricultural Engineering, Jiangsu University for providing all the required instruments without which this work would not have been possible. We would like to express our gratitude to all the reviewers for their patience and help.

Conflicts of Interest: The authors declare no conflicts of interest.

References

1. Hu, Y.; Asante, E.A.; Lu, Y.; Mahmood, A.; Buttar, N.A.; Yuan, S. Review of Air Disturbance Technology for Plant Frost Protection. *Int. J. Agric. Biol. Eng.* **2018**, *11*, 21–28. [CrossRef]
2. Snyder, R.L.; de Melo-Abreu, J.P. *Frost Protection: Fundamentals, Practice and Economics*; Environment and Natural Resources Series; Food and Agriculture Organization of the United Nations: Rome, Italy, 2005; ISBN 978-92-5-105328-7.
3. Kotikot, S.M.; Flores, A.; Griffin, R.E.; Nyaga, J.; Case, J.L.; Mugo, R.; Sedah, A.; Adams, E.; Limaye, A.; Irwin, D.E. Statistical Characterization of Frost Zones: Case of Tea Freeze Damage in the Kenyan Highlands. *Int. J. Appl. Earth Obs. Geoinf.* **2020**, *84*, 101971. [CrossRef]
4. Ru, X.; Zhou, J.; Gong, K.; He, Z.; Dai, Z.; Li, M.; Feng, X.; Yu, Q.; Feng, H.; He, J. Climate Warming May Accelerate Apple Phenology but Lead to Divergent Dynamics in Late-Spring Frost and Poor Pollination Risks in Main Apple Production Regions of China. *Eur. J. Agron.* **2023**, *150*, 126945. [CrossRef]
5. Ru, X.; Jiang, Y.; Luo, Q.; Wang, R.; Feng, X.; Wang, J.; Wang, Z.; Li, M.; Qu, Z.; Su, B.; et al. Evaluating Late Spring Frost Risks of Apple in the Loess Plateau of China under Future Climate Change with Phenological Modeling Approach. *Sci. Hortic.* **2023**, *308*, 111604. [CrossRef]
6. Lu, Y.; Hu, Y.; Li, P. Consistency of Electrical and Physiological Properties of Tea Leaves on Indicating Critical Cold Temperature. *Biosyst. Eng.* **2017**, *159*, 89–96. [CrossRef]
7. Lu, Y.; Hu, Y.; Snyder, R.L.; Kent, E.R. Tea Leaf's Microstructure and Ultrastructure Response to Low Temperature in Indicating Critical Damage Temperature. *Inf. Process. Agric.* **2019**, *6*, 247–254. [CrossRef]
8. Lu, Y.; Asante, E.A.; Duan, H.; Hu, Y. Quantitative Assessment of Cold Injury in Tea Plants by Terahertz Spectroscopy Method. *Agronomy* **2023**, *13*, 1376. [CrossRef]

9. An-Vo, D.-A.; Mushtaq, S.; Zheng, B.; Christopher, J.T.; Chapman, S.C.; Chenu, K. Direct and Indirect Costs of Frost in the Australian Wheatbelt. *Ecol. Econ.* **2018**, *150*, 122–136. [CrossRef]
10. Lou, W.; Zhao, Y.; Huang, X.; Zhu, T.; Yang, M.; Deng, S.; Zhou, Z.; Zhang, Y.; Sun, Q.; Chen, S. Frost Risk Assessment Based on the Frost-Induced Injury Rate of Tea Buds: A Case Study of the Yuezhou Longjing Tea Production Area, China. *Eur. J. Agron.* **2023**, *147*, 126839. [CrossRef]
11. Tang, J.; Wang, P.; Li, X.; Yang, J.; Wu, D.; Ma, Y.; Li, S.; Jin, Z.; Huo, Z. Disaster Event-Based Spring Frost Damage Identification Indicator for Tea Plants and Its Applications over the Region North of the Yangtze River, China. *Ecol. Indic.* **2023**, *146*, 109912. [CrossRef]
12. Cheng, S.; Hu, Y.; Lu, Y.; Pan, Q.; Jin, K.; Zheng, J. Investigation on Combination of Airflow Disturbance and Sprinkler Irrigation for Horticultural Crop Frost Protection. *Agric. Sci.* **2023**, *5*, p8–p15. [CrossRef]
13. Ghaemi, A.A.; Rafiee, M.R.; Sepaskhah, A.R. Tree-Temperature Monitoring for Frost Protection of Orchards in Semi-Arid Regions Using Sprinkler Irrigation. *Agric. Sci. China* **2009**, *8*, 98–107. [CrossRef]
14. Lu, Y.; Hu, Y.; Zhao, C.; Snyder, R.L. Modification of Water Application Rates and Intermittent Control for Sprinkler Frost Protection. *Trans. ASABE* **2018**, *61*, 1277–1285. [CrossRef]
15. Hamer, P.J.C. Simulation of the Effects of Environmental Variables on the Water Requirements for Frost Protection by Overhead Sprinkler Irrigation. *J. Agric. Eng. Res.* **1989**, *42*, 63–75. [CrossRef]
16. Bascietto, M.; Bajocco, S.; Mazzenga, F.; Matteucci, G. Assessing Spring Frost Effects on Beech Forests in Central Apennines from Remotely-Sensed Data. *Agric. For. Meteorol.* **2018**, *248*, 240–250. [CrossRef]
17. Battany, M.C. Vineyard Frost Protection with Upward-Blowing Wind Machines. *Agric. For. Meteorol.* **2012**, *157*, 39–48. [CrossRef]
18. Beyá-Marshall, V.; Herrera, J.; Santibáñez, F.; Fichet, T. Microclimate Modification under the Effect of Stationary and Portable Wind Machines. *Agric. For. Meteorol.* **2019**, *269–270*, 351–363. [CrossRef]
19. Boekee, J.; Dai, Y.; Schilperoort, B.; Van De Wiel, B.J.H.; Ten Veldhuis, M.-C. Plant–Atmosphere Heat Exchange during Wind Machine Operation for Frost Protection. *Agric. For. Meteorol.* **2023**, *330*, 109312. [CrossRef]
20. Doesken, N.J.; Renquist, A.R. A Climatological Assessment of the Utility of Wind Machines for Freeze Protection in Mountain Valleys. *J. Appl. Meteorol. Climatol.* **1989**, *28*, 194–205. [CrossRef]
21. Ribeiro, A.C.; De Melo-Abreu, J.P.; Snyder, R.L. Apple Orchard Frost Protection with Wind Machine Operation. *Agric. For. Meteorol.* **2006**, *141*, 71–81. [CrossRef]
22. Sun, K.; Hu, Y.; Hu, Z.; Chen, Y.; Wei, W. Influence of Frost Protection Windmachine with Continuous Oscillation on Microclimate in Tea Fields. *Agric. Sci.* **2020**, *2*, p236–p242. [CrossRef]
23. Hu, Y.; Liu, P.; Asante, E.; Wu, W.Y.; Li, P.P. Control System of a Performance Test-Bed for Frost Protection Wind Machines. *Int. J. Agric. Biol. Eng.* **2016**, *9*, 36–43. [CrossRef]
24. Yongguang, H.; Chen, Z.; Pengfei, L.; Amoah, A.E.; Pingping, L. Sprinkler Irrigation System for Tea Frost Protection and the Application Effect. *Int. J. Agric. Biol. Eng.* **2016**, *9*, 17–23. [CrossRef]
25. Wenye, W.; Yongguang, H.; Shuo, Y.; Kangqian, M.; Xiaoyong, Z.; Pingping, L. Optimal Design of Wind Machine Impeller for Frost Protection Based on CFD and Its Field Test on Airflow Disturbance. *Int. J. Agric. Biol. Eng.* **2015**, *8*, 43–49. [CrossRef]
26. Wu, W.; Hu, Y.; Lu, H.; Amoah, A.E.; Liu, S. Airfoil Optimization Design for Frost Protection Wind Machines Using Profili Software. *Int. Agric. Eng. J.* **2015**, *24*, 43–51.
27. Wang, J.; Buttar, N.A.; Hu, Y.; Lakhiar, I.A.; Javed, Q.; Shabbir, A. Estimation of Sensible and Latent Heat Fluxes Using Surface Renewal Method: Case Study of a Tea Plantation. *Agronomy* **2021**, *11*, 179. [CrossRef]
28. Buttar, N.A.; Yongguang, H.; Chuan, Z.; Tanny, J.; Ullah, I.; Aleem, M. Height Effect of Air Temperature Measurement on Sensible Heat Flux Estimation Using Flux Variance Method. *Pak. J. Agric. Sci.* **2019**, *56*, 793–800.
29. Hu, Y.; Chen, Y.; Wei, W.; Hu, Z.; Li, P. Optimization Design of Spray Cooling Fan Based on CFD Simulation and Field Experiment for Horticultural Crops. *Agriculture* **2021**, *11*, 566. [CrossRef]
30. Hogg, W.H. Frost Prevention in Dutch Light Frames. *Agric. Meteorol.* **1964**, *1*, 121–129. [CrossRef]
31. Perry, K.B.; Bradley, L. *Frost/Freeze Protection for Horticultural Crops*; North Carolina A&T State University: Greensboro, NC, USA, 1994.
32. Yongguang, H.; Shengzhong, L.; Wenye, W.; Jizhang, W.; Jianwen, S. Optimal Flight Parameters of Unmanned Helicopter for Tea Plantation Frost Protection. *Int. J. Agric. Biol. Eng.* **2015**, *8*, 50–57.
33. Yongzong, L.; Yongguang, H.; Xiliang, Z.; Pingping, L. Responses of Electrical Properties of Tea Leaves to Low-Temperature Stress. *Biol. Eng.* **2015**, *8*, 6.
34. Heusinkveld, V.W.J.; Antoon Van Hooft, J.; Schilperoort, B.; Baas, P.; Veldhuis, M.T.; Van De Wiel, B.J.H. Towards a Physics-Based Understanding of Fruit Frost Protection Using Wind Machines. *Agric. For. Meteorol.* **2020**, *282–283*, 107868. [CrossRef]
35. Kimura, K.; Yasutake, D.; Nakazono, K.; Kitano, M. Dynamic Distribution of Thermal Effects of an Oscillating Frost Protective Fan in a Tea Field. *Biosyst. Eng.* **2017**, *164*, 98–109. [CrossRef]
36. Dai, Y.; Boekee, J.; Schilperoort, B.; Ten Veldhuis, M.-C.; Van De Wiel, B.J.H. Wind Machines for Frost Damage Mitigation: A Quantitative 3D Investigation Based on Observations. *Agric. For. Meteorol.* **2023**, *338*, 109522. [CrossRef]
37. Zhao, T.; Qiao, Z.; Zhang, Y.; Huang, B.; Horton, R.; Liu, G. Experiments and COMSOL Simulations: A Comparative Study of the Heat Flux Plate Method and the Gradient Method for Soil Heat Flux Measurements in Barren Sand. *Agric. For. Meteorol.* **2023**, *334*, 109436. [CrossRef]

38. Lim, H.C. *Optics Modeling and Visualization with COMSOL Multiphysics: A Step by Step Graphical Instruction Manuscripts (Comsol Multiphysics Modeling with Minimum Text)*; CreateSpace Independent Publishing Platform: Scotts Valley, CA, USA, 2018; ISBN 978-1-72451-656-5.
39. Shi, Q.; Liu, D.; Mao, H.; Shen, B.; Li, M. Wind-Induced Response of Rice under the Action of the Downwash Flow Field of a Multi-Rotor UAV. *Biosyst. Eng.* **2021**, *203*, 60–69. [CrossRef]
40. Qin, Z.; Li, Z.; Zou, X.; Guo, Z.; Wang, S.; Chen, Z. Simulation of Starch Gel Printing and Deformation Process Using COMSOL. *Foods* **2024**, *13*, 881. [CrossRef] [PubMed]
41. Crivellini, A.; Ghidoni, A.; Noventa, G. Algebraic Modifications of the K-$\tilde{\omega}$ and Spalart–Allmaras Turbulence Models to Predict Bypass and Separation-Induced Transition. *Comput. Fluids* **2023**, *253*, 105791. [CrossRef]
42. Blazek, J. *Computational Fluid Dynamics: Principles and Applications*; Elsevier: Amsterdam, The Netherlands, 2001; ISBN 978-0-08-054554-7.
43. Wu, J.; Su, X.; Gong, Z.; Cai, J.; Gu, L. Exploration of High-Efficiency Heat Transfer Modes in Lead-Cooled Assemblies: A Structural Optimization Based on the SST k-ω-Kθ-εθ Model. *Appl. Therm. Eng.* **2024**, *247*, 123051. [CrossRef]
44. Uwitonze, H.; Kim, A.; Kim, H.; Brigljević, B.; Vu Ly, H.; Kim, S.-S.; Upadhyay, M.; Lim, H. CFD Simulation of Hydrodynamics and Heat Transfer Characteristics in Gas–Solid Circulating Fluidized Bed Riser under Fast Pyrolysis Flow Condition. *Appl. Therm. Eng.* **2022**, *212*, 118555. [CrossRef]
45. Cicci, L.; Fresca, S.; Guo, M.; Manzoni, A.; Zunino, P. Uncertainty Quantification for Nonlinear Solid Mechanics Using Reduced Order Models with Gaussian Process Regression. *Comput. Math. Appl.* **2023**, *149*, 1–23. [CrossRef]